Apparent dust size discrepancy in aerosol reanalysis in north African dust after long-range transport

Samantha J. Kramer[1], Claudia Alvarez[1], Anne E. Barkley[1], Peter R. Colarco[2], Lillian Custals[1], Rodrigo Delgadillo[1], Cassandra J. Gaston[1], Ravi Govindaraju[2], and Paquita Zuidema[1]

[1]University of Miami, Rosenstiel School of Marine and Atmospheric Science, Miami, FL, USA
[2]NASA Goddard Space Flight Center, Greenbelt, MD, USA

Correspondence: Paquita Zuidema (pzuidema@miami.edu)

Abstract. North African dust reaches the southeast United States every summer. Size-resolved dust mass measurements taken in Miami, Florida indicate that more than one-half of the surface dust mass concentrations reside in particles with geometric diameters less than 2.1 μm, while vertical profiles of micropulse lidar depolarization ratios show dust reaching above four km during pronounced events. These observations are compared to the representation of dust in the MERRA-2 aerosol reanaly-
5 sis and closely-related GEOS-5 Forward Processing (FP) aerosol product, both of which assimilate satellite-derived aerosol optical depths using a similar protocol and inputs. These capture the day-to-day variability in aerosol optical depth well, in a comparison to an independent sun-photometer-derived aerosol optical depth dataset. Most of the modeled dust mass resides in diameters between 2-6 μm, in contrast to the measurements. Modeled-specified mass extinction efficiencies equate light extinction with approximately three times as much aerosol mass, in this size range, compared to the measured dust sizes. GEOS-5
10 FP surface-layer sea salt mass concentrations greatly exceed observed values, despite realistic winds and relative humidities. In combination, these observations help explain, why, despite realistic total aerosol optical depths, 1) free-tropospheric model volume extinction coefficients are lower than those retrieved from the micro-pulse lidar, suggesting too low model dust loadings in the free troposphere, and 2) model dust mass concentrations near the surface can be higher than those measured. The modeled vertical distribution of dust, when captured, is reasonable. Large, aspherical particles exceeding the modeled dust
15 sizes are also occasionally present, but dust particles with diameters exceeding ten μm contribute little to the measured total dust mass concentrations after such long-range transport. Remaining uncertainties warrant a further integrated assessment to confirm this study's interpretations.

1 Introduction

20 Africa contributes almost 50% of the world's dust emissions (Huneeus et al., 2011), with easterly winds transporting the dust over the Atlantic subtropical belt throughout the full seasonal cycle. The impacts of dust span from climate-relevant time scales, which primarily focus on dust's radiative effects, to the shorter time scales important for human endeavours. The latter

include dust storms capable of closing airports, of disrupting military exercises and agriculture, and of human health impacts. The amount of dust mass in diameters less than 2.5 μm in particular is important for air quality, as these can penetrate human lungs (Wilson and Spengler, 1996), setting the diameter threshold used by the United States Environmental Protection Agency in meeting the conditions of the Clean Air Act. Dust mass concentrations in this size range frequently exceed established
5 standards in the Eastern Caribbean (Garrison et al., 2014), if rarely in the southeastern United States (Prospero, 1999b).

The desire for short-term information on dust emissions and their transport has encouraged the dissemination of forecasts through, for example, the World Meteorological Organization's Sand and Dust Storm Warning Advisory and Assessment System. More accurate shorter-term predictions have resulted from a further approach, in which the aerosol forecasts are adjusted by assimilating observed aerosol optical depths (τ_a), primarily derived from satellite. The data assimilation allows
10 global aerosol models to improve the spatial distribution of aerosol plumes and is particularly valuable further away from aerosol source regions, where models tend to underestimate τ_a (Kim et al., 2014; Evan et al., 2014).

A leading global aerosol model also used for operational forecasts is the Goddard Earth Observing System Model Version 5 (GEOS-5), which uses the Goddard Chemistry Aerosol Radiation and Transport (GOCART; Ginoux et al., 2001) scheme. The operational GEOS-5 Forward Processing (FP) model relies on a slightly more mature version of the GEOS-5 model
15 used to produce the global Modern-Era Retrospective analysis for Research and Application-Version 2 (MERRA-2; Randles et al., 2017). For both, the assimilated τ_a, with which the simulated aerosol loadings are adjusted, primarily come from the Moderate Resolution Imaging Spectroradiometer (MODIS) satellite sensor. Any τ_a biases introduced by clouds and other optical inhomogeneities are corrected using a neural network based on surface-based Aerosol Robotic Network (AERONET; Holben et al., 1998) τ_a values as a reference. The better-documented MERRA-2 Reanalysis shows no global bias relative to
20 the surface-derived AERONET τ_a at 550 nm (Gelaro et al., 2017). The assimilation reduces the presence of spurious trends in MERRA-2 (Gelaro et al., 2017) and clearly improves depicted atmospheric aerosol loadings compared to those in non-aerosol-assimilating simulations (Buchard et al., 2017). Importantly for dust transport, the assimilation corrects for a tendency of GEOS-5 to remove dust too quickly from the atmosphere (Buchard et al., 2017), presumably through either excessive sedimentation of the larger particles, or excessive scavenging by clouds.

25 The assimilated τ_a must be redistributed into a vertical structure of the aerosol mass mixing ratio, differentiated between diverse aerosol sources, of which two (dust and sea salt) are further distributed over five size ranges. Mass extinction efficiencies are developed using radiative transfer theory for each of the aerosols and parameterized. These allow the second moment of the size distribution, the vertically-resolved volume extinction coefficient, to be interpreted as the third moment of the size distribution, namely the aerosol mass mixing ratio fundamental to the model. The assimilation allows the model-specified
30 aerosol mass mixing ratios to approximately match the observed τ_a, so that the spatial distribution of the aerosol is improved, with the aerosol source and vertical distribution primarily set by the aerosol parameterizations and model physics. The model physics driving the convective transport, cloud microphysics and mixing influence how much of the aerosol is lofted further, how much is captured by precipitation, how much mixes into the boundary layer, and how much is deposited back to the surface. The particle size and vertical structure distributions are not necessarily independent, as smaller particles will be lofted
35 higher and larger particles will settle out of the atmosphere more quickly. The aerosol size parameterizations therefore have

ramifications for the subsequent transport, the resulting direct radiative effect, and the model aerosol deposition rates. In one comparison of dust vertical profiles, an Aerosol Comparison between Observations and Models (AeroCom) intercomparison of five emission-based models found significant diversity in the modeled vertical dust profiles, with large discrepancies compared to space-based lidar observations (Koffi et al., 2016).

5   Further understanding of the global aerosol model forecasts can be gained from their assessment using *in-situ* and space-based observations. This study assesses the depiction of dust properties after long-range transport within the GEOS-5 FP forecasts and MERRA-2 reanalysis at a location slightly offshore of Miami, Florida, or $\sim$ 6000 km away from the source region. Dust is the dominant aerosol present in the Miami, Florida atmosphere during the summer months (Fig. 1), with sea salt a distant second, even at a coastal site with a consistent sea-salt presence throughout the year (Prospero, 1999a, replotted

10   as the inset in Fig. 1)). Anthropogenic (nitrate, non-sea-salt sulfate) and biogenic (potassium, calcium) mass concentrations are low (Fig. 1). As detailed in many previous studies and easily verified with satellite imagery and the GEOS-5 forecasts, most of the dust originates from northern Africa, with the July maximum in the dust mass concentrations at Miami reflecting a combination of the easterly winds over the remote tropical Atlantic and more southerly winds over the Caribbean (Kramer et al., 2020), and a reduced aerosol removal by precipitation in July compared to August (e.g., v.d. Does et al., 2020). Variability

15   in sea salt mass concentrations can be more directly related to local surface wind speeds. Overall, the dominance of two aerosol species, dust and sea spray, within the summer aerosol environment of Miami, simplifies this study.

2   Background and Datasets

Primary observations include ground-based micropulse lidar (MPL) depictions of the dust vertical structure, surface measurements of bulk and size-resolved dust mass concentrations and sea salt mass concentrations. The daily resolved measurements

20   span three consecutive Miami dust seasons, namely June through September of 2014, 2015 and 2016. The filter and lidar data are collected at the Rosenstiel School of Marine and Atmospheric Science campus of the University of Miami, located on Virginia Key at 25.73°N, 80.16°W, approximately four km east of the Florida mainland. Filter measurements of the bulk mass concentration are made daily from May-September, with more details on the protocol available within Zuidema et al. (2019); these basically follow Prospero (1999a). Further analysis, in support of this study, included analysis of extracts containing the

25   major soluble inorganic ions using the samples from July and August of 2014, primarily to ascertain the sodium mass concentrations. This used flame atomic absorption to determine sodium (Na^+) and suppressed ion chromatography to determine chloride (Cl^-) along with nitrate (NO_3^-) and sulfate ($SO_4^=$) (Savoie et al., 1989). The sea salt concentration is computed from the sodium concentration multiplied by 3.256, following Prospero (1999a). Filter-based dust mass measurements discriminated by size are also collected for 17 select days in 2016 encompassing strong synoptic events. Scanning electron microscopy imag-

30   ing is additionally performed on select filters from this time period. Throughout, the daily dust bulk mass measurements at the surface are matched to the higher time-resolution of lidar measurements. The dust layers and their vertical extent are identified using the MPL polarization capability, and extinction profiles are retrieved from the lidar backscattered intensities for select cases following Delgadillo et al. (2018), with details relevant to this study provided below.

2.1 Size-resolved dust mass concentrations

Dust size distributions are measured on 17 days in 2016 using a Series 230 High Volume Cascade Impactor: Multi-Stage Particulate Size Fractionator manufactured by Tisch Environmental, Inc, following Li-Jones and Prospero (1998). The impactor is located directly below the bulk filters, using a secondary calibrated airflow. Air flow through three aluminum slots discriminates for particle aerodynamic diameters of 10.2, 4.2 and 2.1 μm (see also Table 1) with one final plate capturing the remaining smaller sizes. This helps eliminate particle bounce, wherein dry particles bounce to the subsequent stage (Wang and John, 1987). The high ambient relative humidity of the Miami summer also increases the sticking efficiency of the dust to the impactor surface (Lawson, 1980). The asphericity of dust may introduce an error in the interpretation of each size range, since the impactor selects for the particle size based on only the two horizontal dimensions. The aerodynamic diameter is related here to the smaller geometric diameter through a factor of 0.75 (Kok et al., 2014).

The size-resolved dust masses are thereafter extracted identically to those on the bulk filters. The total dust masses summed from the sized impactor samples agree well with the dust masses from the bulk samples (Fig. 2), lending confidence to the two independent measures. This contrasts with Li-Jones and Prospero (1998), who report dust masses summed from cascade impactors that are one-half to three-quarters of those derived from the bulk samples. A bias towards smaller summed dust masses from impactor samplers is also documented in a more comprehensive assessment of sizing techniques (Reid et al., 2003b). The bias is attributed to aerosol deposition upon the impactor surfaces in both studies, behavior that is thought to be more prevalent for the larger particles, and would thereby emphasize the relative contribution of the smaller sizes to the total dust mass (as will be shown). The lack of a bias between the two total dust mass concentration (Fig. 2) in the present study suggests the lack of bias may be fortuitous, for example, through a difference between the true and assumed air flow.

2.2 Scanning electron microscopy imaging

Scanning electron microscopy imaging is done on filters from August 1 and 2 of 2016, to confirm the size of the largest dust particles and provide insight into the dust geometry. The imaging is conducted on a 1 cm by 1 cm area of the original filter. The samples are coated with palladium in a Cressington-108 Sputter Coater and imaged with a Phillips XL-30/ESEM-FEG at 20kV and 1.6 nA at University of Miami's Center for Advanced Microscopy. The particle size is obtained using ImageJ (https://imagej.nih.gov/ij/). The longest dimension is also referred to as the length (L). The aspect ratio is computed by dividing the L by the width (W) at the longest point that is perpendicular to L (Huang et al., 2020). The aerodynamic diameter (d_a) is calculated from the projected area diameter and the assumption that the particle is a sphere through the use of a volumetric shape factor, aerodynamic shape factor, and particle density from tables for specified oxides based on the chemical composition (Wagner and Leith, 2001; Ott et al., 2008).

2.3 Micropulse lidar

The MPL depolarization capability relies on a toggling between two modes using a polarizing beam splitter, with the ratio of the perpendicularly-polarized to the parallel-polarized radiation at 532 nm wavelength forming the volume linear depolarization

ratio (δ_v). δ_v can be used to distinguish round particles, such as liquid drops and marine aerosols, from particles with distinctive aspherical shapes such as dust. In the free troposphere when dust is the dominant aerosol, the measured δ_v is almost entirely due to dust. For pure near-source dust, Freudenthaler et al. (2009) report a particle linear depolarization ratio (δ_p; this includes a correction for the measured molecular contribution) ratio of 0.31 ± 0.03 at 532 nm. δ_p values for north African dust transported to the Caribbean can be slightly lower (0.30 within Burton et al. (2015) and 0.28 ± 0.02 within Haarig et al. (2017)), although not significantly so. A relatively consistent δ_p throughout transport to the Caribbean can reflect a lack of atmospheric processing (Denjean et al., 2015), in which the externally-mixed dust particles may even increase in asphericity (Huang et al., 2020), although less is known of the chemical composition and shape of dust arriving at Miami via the Gulf of Mexico and subsequent eastward transport over southeastern United States (Kramer et al., 2020).

δ_v is a volume measurement, and when dust is mixed with other aerosols such as sea salt or sulfate, such as will occur in the boundary layer, the measured total δ_v values will be reduced. This can be understood through

$$\delta_v \sim \frac{d_{dust}X}{1 - dX} \text{ where } d_{dust} = \frac{\delta_v}{1+\delta_v} \tag{1}$$

and X is the dust's contribution to the backscattered radiation when no other depolarizing aerosols present (Sugimoto and Lee, 2006). The δ_p of marine salt is approximately 0.05 (Burton et al., 2012), or much lower than that of dust. δ_v values for north African dust after long-range transport range from 0.20 to 0.30 (Kanitz et al., 2014), attributed to mixing with other aerosols. Cloud particles, both liquid and ice, can be distinguished from dust by their higher volume backscatter intensities, with visual imagery from collocated cameras used to discriminate cloudy from cloud-free conditions (Delgadillo et al., 2018).

The Miami MPL was calibrated by the vendor, Sigma Space, prior to its delivery to Miami in 2013, and its calibration and overlap function were checked in 2016 using a mirror to horizontally send and receive the lidar laser beam through the atmosphere, on a day chosen for clear, horizontally-homogeneous conditions. The correction for the near-field overlap occurring within the laser beam is most significant below one km (Delgadillo et al., 2018), and has less influence on measurements of free tropospheric aerosol. The depolarization ratio is not sensitive to the overlap correction. The lidar is kept in a temperature-controlled environment, which reduces fluctuations in the lidar backscatter-to-extinction ratio, and is located approximately 100 m away from where the filter measurements are made. Increases in the volume depolarization ratio from 2015 to 2016 coincide with the incorporation of a new laser diode pump in May, 2016. This will increase the laser beam intensity, increasing the beam's ability to penetrate into the atmosphere, increasing the signal to noise of the signal in both channels (cross- and co-polarization), and ultimately increasing the δ_v value. As such, the volume depolarization ratios reported here serve more as a qualitative indicator for the presence of the dust, than a quantitative measure, although more intense dust events are typically associated with higher volume depolarization ratios (at the same laser intensity), consistent with a higher dust fraction.

The MPL measures a backscattered intensity, which can only be related to the more physically-relevant aerosol volume extinction coefficient through a retrieval that is under-constrained. A sun-photometer-derived aerosol optical depth provides a vertically-integrated constraint on the extinction retrieval (Delgadillo et al., 2018). The two sun photometers, located near the lidar on a rooftop of a three-story building, are part of the Aerosol Robotic Network (AERONET; Holben et al., 1998). The Miami sun photometer version 2 data were calibrated and cloud-filtered (level 2) for 2015 and 2016. The retrieval also

produces a column-average ratio of the backscattered intensity to extinction, known as the lidar ratio. This will also vary with particle size. Because the vertical column above the lidar also contains sea salt in the lower atmosphere, the column-average lidar ratio is not that of the dust in the free troposphere. Lidar ratios at 532 nm range from 40-60 sr for dust and 15-25 sr for sea

5   salt (Burton et al., 2012); a column-average lidar ratio less than that appropriate for dust is consistent with an overestimate in the lidar-retrieved extinction. Optical properties of dust do not vary with relative humidity (Maring et al., 2003a; Denjean et al., 2015), but those for sea salt, a hygroscopic aerosol, will. We estimate the overall uncertainty in the retrieved lidar extinction conservatively with a factor of three. The lidar vertical resolution is 30 m and the time resolution is 15 seconds (done to facilitate detection of the small cumulus clouds common to Miami).

10   ## 2.4   GEOS-5 FP/MERRA-2

The GEOS-5 FP/MERRA-2 products are similar enough that they are used interchangeably within this study, reflecting their incorporation at different times of the study. Aerosol products from the operational GEOS-5 FP model are available at a 25 km grid spacing, slightly finer than the 50 km grid spacing of the global MERRA-2 reanalysis. The GOES-5 model possesses 72 vertical layers, of which the mid-level of the lowest layer is at approximately 69 meters. The aerosol assimilation occurs

15   eight times per day, and the output frequency of the full three-dimensional aerosol field is also every three hours. We primarily consider the dust and sea salt contributions. The GOCART dust emission parameterization depends on a source function, the near-surface wind speeds, and soil moisture (Ginoux et al., 2001). The dust sizes, prescribed at emission, can evolve thereafter during transport, with sedimentation the primary process capable of altering the dust size distribution (the dust is non-hygroscopic). The parameterization of the dust mass distribution by size approximately follows that of Tegen and Lacis

20   (1996) and contains five size categories, extending to a maximum diameter of 20 μm. These are indicated in Table 1 along with the density and mass extinction efficiency (ratio of extinction to mass) corresponding to each size category. Spheroidal particles are assumed, with more details on the dust parameterization available in Colarco et al. (2010).

The flux of sea salt off of the ocean surface is also parameterized into five size bins, but the size is allowed to vary with the surface wind speeds and sea surface temperature, and the sea salt can undergo hygroscopic growth as a function of the relative

25   humidity. The sea salt parameterization is adapted from Gong (2003) and described further in Chin et al. (2002) and Bian et al. (2019).

The clear-sky τ_a values at a wavelength of 550 nm are primarily assimilated from the Moderate Resolution Imaging Spectroradiometer (MODIS) and secondarily the Multi-Angle Imaging SpectroRadiometer (MISR) satellite instruments (Randles et al., 2017). Data from the surface-based AERONET sites are no longer assimilated (Arlindo da Silva, personal communica-

30   tion) allowing the Miami sun photometer data to independently validate the GEOS-5 FP τ_a. The lowest model level is assumed to represent surface values. Inspection of the MERRA-2 and GEOS-5 FP dust and sea salt profiles for the cases shown in Fig. 11 revealed little difference between the two products.

2.5 HYSPLIT back trajectories

Daily average back-trajectories explore the differences in the integrated air flow for days with high and low dust mass concentrations. The calculations rely on the NOAA Air Resources Laboratory HYSPLIT model (Stein et al., 2015). These extend for 300 hours (12.5 days) and are driven by the NCEP Reanalysis Climate Diagnostics Center-1 product. Each day's trajectory is initialized at 00Z and at an altitude of 2000 m. This is a robust height for the presence of dust above Miami, as indicated later. There is some evidence that the NCEP Reanalysis lower tropospheric winds may be weaker than observed (e.g., Adebiyi et al., 2015), which would increase the transport time, but this is not investigated further for this study.

3 Overview of 2014-2016 summer dust seasons

A time series of the primary measurements displays the daily surface-based filter-derived dust mass concentrations and the corresponding vertical structure as captured by the lidar volume depolarization ratio, for each of the three dust seasons (Fig. 3). The lidar measurements indicate that dust is often prevalent in the boundary layer, typically extends up to 2-3 km, and occasionally rises above 4 km but not above 5 km. The depolarization ratios indicate that when dust is present, it is typically also present within the boundary layer. This is corroborated by the filter measurements; only during mid-to-late August 2015 is no dust detected within the atmospheric column by either the filters or the lidar. The synoptic and year-to-year variability is clear, with the highest dust mass concentrations occurring on just a few select days of each summer. In 2014, these occur in August, and in 2015 and 2016, during July, dominating the monthly-means for those years. Less dust in June than July, in contrast to Barbados (Zuidema et al., 2019) reflects more strongly zonal flow in June (Kramer et al., 2020), while the decrease in August can also reflect increased removal by precipitation en route (v.d. Does et al., 2020).

The back-trajectories indicate the crucial role of the north Atlantic subtropical high in guiding the atmospheric flow towards Miami (Fig. 4a-c), explored further in Kramer et al. (2020). Many back-trajectories intersect the north African coast, with few continuing further eastward over the African continent. This may indicate a strong influence from the northerly coastal flow on the eastward side of the north Atlantic subtropical high. The HYSPLIT back-trajectories disregard explicit mixing with environmental air, but a back-trajectory with a large meridional component would imply more mixing of the dusty air with air emanating from the northeast Atlantic and Europe. The separate influences of African versus Atlantic air on Miami and Caribbean thermodynamic profiles are also noted in Dunion (2011).

After twelve days, the integration confidence in the trajectories leading to the original location of air parcel is debatable, therefore we focus more on the trajectory characteristics over the Atlantic. Back-trajectories associated with days with dust mass concentrations exceeding 20 μg m^{-3} are typically more zonal, suggesting less mixing with air originating from the northeastern Atlantic. Back trajectories associated with days with high dust mass concentrations also have a slight preference for a more northerly location. This may indicate less aerosol removal by precipitation en route (the northern boundary of the June-August intertropical convergence zone is at approximately 10° N). A notable feature of the back-trajectories on days with low (< 1 μg m^{-3}) and moderate (1 - 20 μg m^{-3}) dust mass concentrations in Miami is a less direct transport of dust, with the back-trajectories passing over the Gulf of Mexico and then recirculating back to Miami via the lower southeast United States.

This is most evident in 2014 and 2015. This transport pathway is effective at dispersing dust over large areas of southeastern
5 United States, and increases the likelihood of dust interacting with other terrestrial and anthropogenic aerosols en route.

4 Comparison of GEOS-5 FP/MERRA-2 aerosol distributions to the Miami observations

4.1 Aerosol optical depth

The GEOS-5 FP τ_a values (at 550 nm wavelength) slightly exceed those from the sun photometers (at 500 nm) at optical
depths below 0.15, and are slightly less for $\tau_a > 0.15$ (Fig. 5). The slight underestimation at higher τ_a has previously been
10 attributed to missing emissions (Buchard et al., 2017; Shi et al., 2019). It is also apparent in a comparison of MERRA-2 τ_a
to shipborne τ_a observations (Fig. 9 of Randles et al., 2017). Surface albedo inhomogeneities at this coastal location could
perhaps contribute to the overestimate at the lowest τ_a, although another interpretation, shown next, is that an overestimate
from the sea salt contribution becomes most apparent at the lowest τ_a. An implication of the positive correlation (coefficient of
0.80), overall, is that the AERONET cloud screening is effective. Although not shown, the day-to-day variations in τ_a match
15 well, as would be expected given the assimilation and availability of satellite-derived τ_a.

4.2 Surface sea salt mass concentrations

A first step within the assimilation scheme is the aerosol speciation, and how much of the aerosol is partitioned into sea salt
will also affect the amount available for dust. The GEOS-5 FP aerosol product overestimates the near-surface salt mass con-
centration by an order of magnitude, with a model mean value of 61 μg m^{-3} versus a measured mean salt mass concentration
20 of 7.7 μg m^{-3} estimated from the sodium measurements (Fig. 6). The latter is consistent with previous measurements (Savoie
and Prospero, 1982; Prospero, 1999a). Further assessment of the GEOS-5 wind speeds and relative humidity using surface
meteorological data indicate that these are realistic (not shown), suggesting that the underlying size and/or light extinction pa-
rameterizations may be the issue. This is consistent with the findings of Bian et al. (2019), in which an inconsistency between
an overpredicted salt mass concentration and underpredicted $\tau_{seasalt}$ in GOES-5 simulations is reconciled through the model
25 adoption of too-large sea salt sizes. As noted by Buchard et al. (2017), the assimilation of aerosol optical depths that exceed
those forecast can further exacerbate the discrepancy.

4.3 Surface dust mass concentrations

All else equal, an overestimate of the GEOS-5 FP sea salt mass concentrations might point to GEOS-5 FP dust mass con-
centrations that are too low, for the same assimilated aerosol optical depth. Instead, the GEOS-5 FP near-surface dust mass
30 concentrations also exceed observed values on almost two-thirds of the days, for a mean bias of 3.46 μg m^{-3} (Fig. 7). This
overestimation is not as pronounced as that for sea salt. A clear correlation (value of 0.63) is apparent, matching that reported
in Buchard et al. (2017) based on Barbados measurements; Buchard et al. (2017) did not find a bias between MERRA2 and
the Barbados dust mass concentrations. GEOS-5 FP approximately captures the monthly evolution from July to September,

although the GEOS-5 FP overestimate is most pronounced for June, when it is enough to alter the perception of the monthly evolution (i.e. the GEOS-5 FP maximum in 2014 and 2016 occurs in June, in contrast to a July (August) maximum in the observations). The cause for this is unclear.

The model overestimate in the surface dust mass concentrations has consequences for inferences of the frequency of high and low dust loading days (Fig. 8). Measured dust mass concentrations exceeding 40 μg m^{-3} or less than 1 μg m^{-3} were infrequent, with dust present in the Miami boundary layer at concentrations between 1 to 10 μg m^{-3} over one-half of the time. In contrast, GEOS-5 FP include more days with concentrations exceeding 10 μg m^{-3} than are observed, and correspondingly fewer days with concentrations between 1-10 μg m^{-3}. GEOS-5 FP overall places too much dust in the boundary layer. The consistent presence of dust in the boundary layer in and of itself is not controversial, see Reid et al. (2002) for example, as well as Fig. 3.

4.4 Does dust size explain the difference between the GEOS-5 FP/MERRA-2 and measured dust mass concentrations?

The use of a size distribution parameterization that permits a larger mass for the same visible extinction (as is thought to occur for sea salt; Bian et al. (2019)) is one explanation for why the MERRA-2 dust mass concentrations near the surface may exceed those observed, despite realistic assimilation-constrained aerosol optical depths. This idea is assessed using the size-resolved dust mass concentrations from 17 days in 2016. The 28 July to 9 August time period included one of the heaviest and longest dust mass concentration events from 2016, and data from another dust event spanning 1-2 September are also included. The trajectories for these days indicate direct dust transport from northern Africa. The subtropical high was strongest and located furthest north in 2016 of the three years considered, based on the 1023 hPa sea level pressure contour (Fig. 4). This may have decreased dust transport that year (Kramer et al., 2020), resulting in relatively fewer days with dust exceeding 20 μg m^{-3} for that year. The episodic-maximum dust mass concentration of 28 μg m^{-3} occurred on August 4, 2016 (Fig. 2). The days with the largest size particles (7/30, 8/2, and 8/4) correspond to high lidar volume depolarization ratios and larger total bulk surface dust mass concentrations (Fig. 3).

The comparison is eased by first estimating the geometric diameter corresponding to the measured aerodynamic particle diameter, and thereafter normalizing both size-resolved dust mass concentrations into diameter bins with a 2 μm width (Fig. 9). The measurements place approximately two-thirds of the total dust mass concentrations in particles with geometric diameters < 2 μm, with the presence of some larger particles resulting in a mass-weighted mean measured diameter of 3.0 μm. In contrast, GEOS-5 FP places approximately one-fourth of the dust into diameters < 2 μm, and approximately 45% into the 2-6 μm diameter range, with almost no mass in larger diameters. The GEOS-5 FP mass-weighted mean diameter is thus larger than observed, at 3.9 μm. An important caveat with the cascade impactor measurements is that the larger dust particles are less likely to be captured (Li-Jones and Prospero, 1998; Reid et al., 2003b), with other studies concluding that one-third to one-half of the total dust mass is in diameters < 2 (or 2.5) μm (Perry et al., 1997; Li-Jones and Prospero, 1998; Prospero et al., 2001).

Even with a relative potential overestimation of the smaller particle sizes, the enhanced ability of particles with diameters < 2 μm to scatter sunlight, indicated by mass extinction efficiencies that exceed by at least a factor of three those for larger particles

(Table 1), implies that more mass is required to produce the same extinction for larger particles than for smaller particles. Fig. 9 indicates that one cause for the overestimated near-surace dust mass concentrations in GEOS-5 FP above southern Florida may

5 be a dust size parameterization that distributes more of the dust mass into a larger size, for which the mass extinction efficiency is lower, than is observed.

As highlighted by the inset to Fig. 9, in which the size-resolved dust mass distributions are shown on a logarithmic scale, more of the measured mass is contained in particles with diameters > 6 μm, than in the model (10% versus 4%). An underestimation of the largest dust sizes in global models and its implications has been examined in Adebiyi and Kok (2020)

10 and references therein. Filters from 1 and 2 August indicate mass from particles with diameters > 10 μm, and these were interrogated further with scanning electron microscopy to independently corroborate the particle size (Fig. 10). Four of the five examples include a dimension exceeding 20 μm (see Table 2 for dimensions of each identified particle), with the largest particle measuring 36.4 by 26.8 μm (Fig. 10b). The aerodynamic diameters (d_a) confirm that the appropriate impactor stage is indeed collecting particles with $d_a > 10$ μm (See Table 2). The particles are highly aspherical, with aspect ratios ranging

15 from 1.36 to 2.6. Although these are only five samples, their mean aspect ratio of 1.9 is equal to the median calculated from almost 78000 samples gathered in Puerto Rico (Reid et al., 2003a, b; Huang et al., 2020). This asphericity will contribute to the survival of the particles, as aspherical particles fall at slower terminal speeds than spheres of equivalent mass (Yang et al., 2013; Huang et al., 2020). These observed dust particles exceed the GEOS-5 upper limit of a 20 μm diameter. However, only 0.45 μg m^{-3} of the total measured dust mass concentration (approximately 3%) is contained in particles with diameters exceeding

20 10 μm, implying that the neglect of particles with diameters > 20 μm by GEOS-5 FP only results in a small error in the total dust mass concentration after such long-range transport.

4.5 Dust vertical structure

The extinctions corresponding to the GEOS-5 FP dust mass mixing profiles, estimated using the mass extinction efficiencies specific to each size range (Table 1), can be assessed using extinctions retrieved from the lidar backscattered intensities (Del-

25 gadillo et al., 2018). This is similar to the strategy invoked within Liu et al. (2012) for comparison between space-based lidar extinctions and GEOS-5 dust mass loadings, using a mass extinction efficiency of 0.7 m^2 g^{-1}, and Sauter et al. (2019) (who use a smaller value of 0.4 m^2 g^{-1}, implying larger particles). Four examples, spanning the 28-30 July 2016 dust event and that of 5 August, 2016, are shown in Fig. 11. The AERONET-derived τ_a from the early morning, overlapping with 12 UTC, indicate values of 0.1-0.2, with the highest aerosol loading occurring on 29 July, 2016.

30 The time series of the lidar-derived extinctions (Fig. 11c,f,i and l, all corresponding to nighttime when the lidar signal is more robust) indicate dust extending up to 4 km at times, stratified into distinct layers supporting what appear to be gravity waves (Fig. 11). A peak at 2 km is specific to the 28-30 July dust event (Fig. 3), and a secondary peak at approximately 800 m represents the boundary layer top, where the maximum in relative humidity may induce the hygroscopic swelling of sea spray aerosols, or indicate undetected optically-thin cloud (Delgadillo et al., 2018). The GEOS-5 FP dust mass concentrations clearly indicate the presence of dust in the free troposphere on two of the days, though, perhaps surprisingly, not on the day with the highest AERONET-derived optical depth. When dust is present, its distribution by altitude is similar to that inferred

from the lidar. Within the boundary layer, the filter-based size-resolved dust mass concentrations measurements (thick red bars within Fig 11a,d,g and j) reach 10 μg m^{-3} or more on all four days. GEOS-5 FP near-surface dust mass concentration values

5   are higher on all four days than those measured (compare to the thick black bars).

    Corresponding model aerosol extinction profiles, resolved over the 3-12 UTC time frame encapsulated within the average of the cloud-free lidar extinction profiles, suggests that the GEOS-5 FP product does not distribute enough of the assimilated τ_a above 1.5 km on any of the four days (Fig. 11b,e,h,k). Most of the model τ_a is confined to the boundary layer, where the τ_a also contains a sea spray contribution given relative humidities capable of exceeding 80% (not shown). The lidar extinction

10 values within the boundary layer are much lower than those from GEOS-5 FP, despite including a sea salt contribution, and, are also lower in the free troposphere compared to those derived using GEOS-5 values.

    A further assessment examines whether GEOS-5 preferentially places larger particles at lower altitudes, based on larger fall speeds for larger sizes, as this may contribute to the lower model-estimated dust extinctions. Size-resolved model dust mass mixing ratios for 28 July 2016 indicate that larger particles do prefer lower altitudes (Fig. 12), and in particular much fewer

15 particles with diameters > 6 μm occur above the boundary layer. In the two size ranges with the largest discrepancy between the model and measurements (2-4 μm versus 0.2-2 μm), the altitude difference between the vertical distribution of the two size-resolved dust mass mixing ratios is only on the order of 100-300 m, however.

    To summarize, this assessment indicates that GEOS-5 FP places too much dust within the boundary layer, and possibly not enough in the free troposphere above the boundary layer, although mass measurements in the free troposphere are lacking with

20 which to more definitely validate the latter claim. Where GEOS-5 FP does place dust within the free troposphere, the mass is reasonably distributed by altitude.

5   Conclusions and Discussion

Dust forecasts incorporating the assimilation of satellite-derived τ_a can circumvent a difficulty global aerosol models encounter, in which τ_a is too low further away from a source region (e.g., Kim et al., 2014; Evan et al., 2014; Ansmann et al., 2017). As

25 such, the assimilation of observed τ_a holds the promise of more accurate depictions of the global aerosol distribution. While the GEOS-5 FP aerosol forecasts and MERRA-2 capture independently-measured τ_a and its spatial variability well for an aerosol environment dominated by sea spray and long-range dust, the more challenging objective of a realistic aerosol vertical distribution, in both size and mass, is less well met. A clear overestimate in the modeled sea salt loading, apparent in an *in situ* comparison (Fig. 6) is corroborated by the independent findings of Bian et al. (2019). This will foster an underestimate in the

30 dust loading, for the same assimilated τ_a.

    A comparison to dust mass concentrations measured at the surface and to lidar profiles of retrieved extinction indicates that GEOS-5 FP can distribute dust too low in the atmosphere, with too much mass placed in particle sizes that are larger than observed (except at the largest sizes). An overestimate of the amount of dust in the boundary layer has implications for model-deduced ocean fertilization by the soluble iron (e.g. Colarco et al., 2003), and for cloud nucleation. Size-resolved measurements place most of the mass in diameters smaller than 2 μm, while GEOS-5 FP/MERRA-2 places most of the dust

mass in diameters between 2 to 4 μm (Fig. 9). The prescribed dust mass extinction efficiency, by which the dust portion of the assimilated aerosol optical depth is cast as a dust mass mixing ratio, is more than a factor of 3 larger for the smaller size

5 (Table 1), and small differences in the distribution of mass between 0-2 μm and 2-4 μm has significant ramifications for the extinction. A model dust size distribution that places more of the dust in slightly larger sizes, will overestimate the dust mass even if the light extinction by dust is correctly represented.

  The overestimate in the model dust size after long-range transport is opposite to that documented for most global aerosol models, in which the number of small particles can be overestimated relative to the large particles (e.g., Kok, 2011). We

10 recognize a recent emphasis on the presence of very large dust particles within the Saharan Air Layer (e.g., Ryder et al., 2019), and their ability to be transported for long distances. Large aspherical dust particles are also detected at Miami after a transport of $\sim$ 6000 km, exceeding the amount modeled, but their contribution to the overall mass is negligible. Their presence is consistent with other observations that perceive little mixing of African dust with other air masses en route for select cases (Karyampudi et al., 1999), and find larger dust particles closer to the top of the Saharan air layer (Jung et al., 2013; Yang et al.,

15 2013; Gasteiger et al., 2017), as opposed to the bottom. The existence of the large particles may be more typical of the dust events that advect more directly to Miami and undergo little precipitation. The neglect of particles exceeding the maximum GEOS-5-specified particle diameter of 20 μm introduces little error in the total GEOS-5 dust mass concentrations, but may be more important for the direct aerosol radiative effect, in particular the longwave component. This is not addressed here.

  A previous study focusing on dust size distributions in coastal Florida indicates relatively fewer dust particles with diameters

20 < 2 μm than are reported here (Prospero et al., 2001), and the cascade impactor may be prone to undersampling the largest sizes (Li-Jones and Prospero, 1998; Reid et al., 2003b), although the good correspondence to the bulk measurements argues against this. Cloud processing in the boundary layer will also preferentially remove the largest dust particles. A survey of other measured dust sizes reported in the literature reinforces that dust particle sizes can be difficult to compare in a consistent manner across studies. Kok et al. (2017) indicate that most of the north African dust mass at emission is contained in particle diameters

25 reaching 10 μm. Ryder et al. (2013) report that most of their dust mass, in measurements made close to the African coast, is in diameters exceeding 5 μm, consistent with Haywood et al. (2003). Closer to coastal Florida, *in-situ* measurements made during the Puerto Rico Dust Experiment place most of the mass in particles with diameters between 5-7 μm (Maring et al., 2003b; Reid et al., 2003c), with similar sizes between the boundary layer and the free troposphere (Maring et al., 2003a). The Denjean et al. (2015) study, also based on measurements taken in Puerto Rico, does not consider particle diameters < 1 μm. In contrast,

30 inferences of dust size deduced from multi-wavelength lidar measurements at Barbados (Haarig et al., 2017) estimate most dust particles are 1.6-2.0 μm in diameter, which is more broadly consistent with the Miami impactor measurements. Other recent lidar measurements also perceive larger concentrations of aerosols with diameters < 2 μm (Haarig et al., 2019). This is at first glance consistent with the *in-situ* dust mass concentrations reported in Jung et al. (2013) near Barbados, but these do not extend beyond 2.5 μm in diameter (most aircraft aerosol intake inlets cut off at 3 μm), and do not resolve the larger sizes.

35 Our dust size measurements are gathered at a location further away from the dust source than Puerto Rico (Reid et al., 2002, 2003a, c; Maring et al., 2003a, b) and Barbados (Jung et al., 2013; Weinzierl et al., 2016), although effort was made to select for those days with a more direct transport from northern Africa (as opposed to resulting from a recirculation around

the Gulf of Mexico). Reasons for the size discrepancy between our measurements and those produced by GEOS-5 FP remain not entirely understood. Critiques can be made of each individual measurement presented within this study. In their totality, however, a consistent interpretation emerges based on the retrieved lidar extinctions, and near-surface dust and sea salt mass concentrations, suggesting the model mean dust sizes, by mass, are too large, leading to relatively too much dust mass placed in the boundary layer. At the same time, the total dust loading is too low within GEOS-5 FP and MERRA-2, possibly because too much of the assimilated aerosol optical depth is speciated into sea salt. We consider the current analysis a pilot study, however, and recommend a further dedicated assessment with a multi-wavelength depolarization extinction lidar as well as a more complete set of size-resolved *in-situ* dust mass measurements, both at the ground and in the free troposphere. This will better anchor ideas for future improvements to the depiction of the full dust lifecycle within the GEOS-5 model, including through wet deposition.

Data availability. The datasets developed for this study (lidar extinction retrievals, size-resolved dust mass concentrations and measured sodium mass concentrations) are available from the University of Miami Scholarly Repository at https://doi.org/10.17604/1b5v-h184. These include the sun photometer aerosol optical depths, which are also publicly available through the AERONET website. The bulk dust mass concentration dataset is available through the University of Miami Scholarly Repository at https://doi.org/10.17604/q3vf-8m31, for which Zuidema et al. (2019) is the appropriate reference. The HYSPLIT model can be accessed through https://www.ready.noaa. gov/HYSPLIT.php, a NOAA Air Resource Laboratory product.

Author contributions. PZ designed the study and led the writing of the manuscript. SK carried out the data collection and initial analysis and drafted the initial manuscript. The GEOS-5 FP and MERRA2 values were provided by RG. RD provided the lidar analysis. CA contributed to the Miami data collection, with LC providing input on the methodology and additional mentorship of SK. AB provided the SEM analysis. PC provided substantial insight into the GEOS-5 and MERRA2 methodology. All authors commented on the manuscript.

Competing interests. No competing interests are present

Acknowledgements. We gratefully acknowledge support for the acquisition of the micropulse lidar and sun photometers through an NSF Major Research Instrumentation grant 0923217. PZ, SK and CA acknowledge additional support from a Faculty Program Fund, NSF AGS-1233874 and an NSF AGS Research Experiences for Undergraduates grant. We thank Arlindo da Silva for intellectual input on the original study. RD acknowledges support from DOE ASR grant DE-SC0013720. We thank Brent Holben and Tom Eck for their support of the Miami sun photometers through the AERONET project. Jasper Kok and an additional anonymous reviewer are thanked for their thoughtful comments, which helped improve the manuscript. This work would not have been possible without the history of investments by Dr. Joseph Prospero into the dust filter sampling program at U of Miami, its analysis and intellectual interpretation.

References

Adebiyi, A., Zuidema, P., and Abel, S.: The convolution of dynamics and moisture with the presence of shortwave absorbing aerosols over the southeast Atlantic, J. Clim., 28, 1997–2024, https://doi.org/10.1175/JCLI-D-14-00352.1, 2015.

Adebiyi, A. A. and Kok, J. F.: Climate models miss most of the coarse dust in the atmosphere, Sci. Adv., 6, eaaz9507, 2020.

Ansmann, A., Rittmeister, F., Engelmann, R., Basart, S., Jorba, O., Spyrou, C., Remy, S., Skupin, A., Baars, H., Seifert, P., Senf, F., and Kanitz, T.: Profiling of Saharan dust from the Caribbean to western Africa – Part 2: Shipborne lidar measurements versus forecasts, Atmos. Chem. Phys., 17, 14 987–15 006, https://doi.org/10.5194/acp-17-14987-2017, https://www.atmos-chem-phys.net/17/14987/2017/, 2017.

Bian, H., Froyd, K., Murphy, D. M., Dibb, J., Darmenov, A., Chin, M., Colarco, P. R., da Silva, A., Kucsera, T. L., Schill, G., Yu, H., Bui, P., Dollner, M., Weinzierl, B., and Smirnov, A.: Observationally constrained analysis of sea salt aerosol in the marine atmosphere, Atmos. Chem. Phys., 19, 10 773–10 785, https://doi.org/10.5194/acp-19-10773-2019, https://www.atmos-chem-phys.net/19/10773/2019/, 2019.

Buchard, V., Randles, C. A., da Silva, A. M., Darmenov, A., Colarco, P. R., Govindaraju, R., Ferrare, R., Hair, J., Beyersdorf, A. J., Ziemba, L. D., and Yu, H.: The MERRA-2 Aerosol Reanalysis, 1980 Onward. Part II: Evaluation and Case Studies, J. Climate, 30, 6851–6872, https://doi.org/10.1175/JCLI-D-16-0613.1, https://doi.org/10.1175/JCLI-D-16-0613.1, 2017.

Burton, S. P., Ferrare, R. A., Hostetler, C., Hair, J. W., Rogers, R. R., Obland, M., Butler, C., Cook, A., Harper, D., and Froyd, K.: Aerosol classification using airborne High Spectral Resolution Lidar measurements – methodology and examples, Atmos. Meas. Tech., 5, 73–98, https://doi.org/10.5194/amt-5-73-2012, https://www.atmos-meas-tech.net/5/73/2012/, 2012.

Burton, S. P., Hair, J. W., Kahnert, M., Ferrare, R. A., Hostetler, C. A., Cook, A., Harper, D. B., Berkoff, T. A., Seaman, S. T., Collins, J. E., Fenn, M., and Rogers, R.: Observations of the spectral dependence of linear particle depolarization ratio of aerosols using NASA Langley airborne High Spectral Resolution Lidar, Atmos. Chem. Phys., 15, 13 453–13 473, https://doi.org/10.5194/acp-15-13453-2015, 2015.

Chin, M., Ginoux, P., Kinne, S., Holben, B. N., Duncan, B. N., Martin, R., , Logan, J., Higurashi, A., and Nakajima, T.: Tropospheric aerosol optical thickness from the GOCART model and comparisons with satellite and sun photometer measurements, J. Atmos. Sci., 59, 461–483, 2002.

Colarco, P., da Silva, A., Chin, M., and Diehl, T.: Online simulations of global aerosol distributions in the NASA GEOS-4 model and comparisons to satellite and ground-base d aerosol optical depth, J. Geophys. Res., 115, https://doi.org/10.1029/2009JD012820, d14207, 2010.

Colarco, P. R., Toon, O. B., Reid, J. S., Livingston, J. M., Russell, P. B., Redemann, J., Schmid, B., Maring, H. B., Savoie, D., Welton, E. J., Campbell, J. R., Holben, B. N., and Levy, R.: Saharan dust transport to the Caribbean during PRIDE: 2. Transport, vertical profiles, and deposition in simulations of in situ and remote sensing observations, J. Geophys. Res., 108, 8590–8606, https://doi.org/10.1029/2002JD002659, 2003.

Colarco, P. R., Nowottnick, E. P., Randles, C., Yi, B., Yang, P., Kim, K.-M., Smith, J. A., and Bardeen, C. G.: Impact of radiatively interactive dust aerosols in the NASA GEOS-5 climate model: Sensitivity to dust particle shape and refractive index, J. Geophys. Res., 119, 753–786, https://doi.org/10.1002/2013JD020046, 2014.

Delgadillo, R., Voss, K., and Zuidema, P.: Characteristics of optically-thin coastal Florida cumuli from surface-based lidar measurements, J. Geophys. Res., 123, 10,591–10,605, https://doi.org/10.1029/2018JD028867, 2018.

Denjean, C., Caquineau, S., Desboeufs, K., Laurent, B., Maille, M., Rosado, M. Q., Vallejo, P., Mayol-Bracero, O. L., and Formenti, P.: Long-range transport across the Atlantic in summertime does not enhance the hygroscopicity of African mineral dust, Geophys. Res. Lett., 42, 7835–7843, 2015.

Dunion, J.: Rewriting the climatology of the tropical North Atlantic and Caribbean Sea atmosphere, J. Clim., 24, https://doi.org/10.1175/2010jcli3496.1, 2011.

15 Evan, A. T., Flamant, C., Fiedler, S., and Doherty, O.: An analysis of aeolian dust in climate models, Geophys. Res. Lett., 41, 5996–6001, https://doi.org/10.1002/2014GL060545, 2014.

Freudenthaler, V., Esselborn, M., Wiegner, M., Heese, B., Tesche, M., Ansmann, A., Müller, D., Althausen, D., Wirth, M., Fix, A., Ehret, G., Knippertz, P., Toledano, C., Gasteiger, J., Garhammer, M., and Seefeldner, M.: Depolarization ratio profiling at several wavelengths in pure Saharan dust during SAMUM 2006, Tellus, 61, 165–179, https://doi.org/10.1111/j.1600-0889.2008.00396.x, 2009.

20 Garrison, V. H., Majewski, M., Foreman, W. T., Genualdi, S. A., Mohammed, A., and Simonich, S. L.: Persistent organic contaminants in Saharan dust air masses in West Africa, Cape Verde and the eastern Caribbean, Science Tot. Env., pp. 468–469, https://doi.org/10.1016/scitotenv.2013.08.076, http://dx.doi.org/10.1016/j.scitotenv.2013.08.076, 2014.

Gasteiger, J., Groß, S., Sauer, D., Haarig, M., Ansmann, A., and Weinzierl, B.: Particle settling and vertical mixing in the Saharan Air Layer as seen from an integrated model, lidar, and in situ perspective, Atmos. Chem. Phys., 17, 297–311, https://doi.org/10.5194/acp-17-297-2017,

25 https://www.atmos-chem-phys.net/17/297/2017/, 2017.

Gelaro, R., McCarty, W., Suárez, M. J., Todling, R., Molod, A., Takacs, L., Randles, C. A., Darmenov, A., Bosilovich, M. G., Reichle, R., Wargan, K., Coy, L., Cullather, R., Draper, C., Akella, S., Buchard, V., Conaty, A., da Silva, A. M., Gu, W., Kim, G.-K., Koster, R., Lucchesi, R., Merkova, D., Nielsen, J., Partyka, G., Pawson, S., Putman, W., Rienecker, M., Schubert, S. D., Sienkiewicz, M., and Zhao, B.: The Modern-Era Retrospective Analysis for Research and Applications, Version 2 (MERRA-2), J. Clim., 30, 5419–5454,

30 https://doi.org/10.1175/JCLI-D-16-0758.1, https://doi.org/10.1175/JCLI-D-16-0758.1, 2017.

Ginoux, P., Chin, M., Tegen, I., Prospero, J., Holben, B., Dubovik, O., and Lin, S.-J.: Sources and distributions of dust aerosols simulated with the GOCART model, J. Geophys. Res., 106, 20 255–20 273, https://doi.org/10.1029/2000JD000053, 2001.

Gong, S.: A parameterization of sea-salt aerosol source function for sub- and super-micron particles, Global Biogeochem. Cycles, 17, 1097–1106, https://doi.org/10.1029/2003GB002079, 2003.

35 Haarig, M., Ansmann, A., Althausen, D., Klepel, A., Groß, S., Freudenthaler, V., Toledano, C., Mamouri, R.-E., Farrell, D. A., Prescod, D. A., Marinou, E., Burton, S., Gasteiger, J., Engelmann, R., and Baars, H.: Triple-wavelength depolarization-ratio profiling of Saharan dust over Barbados during SALTRACE in 2013 and 2014, Atmospheric Chemistry and Physics, 17, 10 767–10 794, https://doi.org/10.5194/acp-17-10767-2017, https://www.atmos-chem-phys.net/17/10767/2017/, 2017.

Haarig, M., Walser, A., Ansmann, A., Dollner, M., Althausen, D., Sauer, D., Farrell, D., and Weinzierl, B.: Profiles of cloud condensation nuclei, dust mass concentration, and ice-nucleating-particle-relevant aerosol properties in the Saharan Air Layer over Barbados from polarization lidar and airborne in situ measurements, Atmos. Chem. Phys., 19, 13 773–13 788, https://doi.org/10.5194/acp-19-13773-2019, https://www.atmos-chem-phys.net/19/13773/2019/, 2019.

5 Haywood, J., Francis, P., Osborne, S., Glew, M., Loeb, N., Highwood, E., Tanre', D., Myhre, G., Formenti, P., and Hirst, E.: Radiative properties and direct radiative effect of Saharan dust measured by the C-130 aircraft during SHADE: 1. Solar spectrum, J. Geophys. Res., 108, 8577–8593, https://doi.org/10.1029/2002JD002687, 2003.

Holben, B. N., Eck, T., Slutsker, I., Tanré, D., Buis, J. P., Setzer, A., Vermote, E., Reagan, J. A., Kaufman, Y. J., Nakajima, T., Lavenu, F., Jankowiak, I., and Smirnov, A.: AERONET- A Federated Instrument Network and Data Archive for Aerosol Characterization, Remote

10 Sens. Environ., 66, 1–16, https://doi.org/10.1016/S0034-4257(98)00031-5, 1998.

Huang, Y., Kok, J. F., Kandler, K., Lindqvist, H., Nousiainen, T., Sakai, T., Adebiyi, A., and Jokinen, O.: Climate Models and Remote Sensing Retrievals Neglect Substantial Desert Dust Asphericity, Geophys. Res. Lett., 47, e2019GL086592, 2020.

Huneeus, H., Schulz, M., Balkanski, Y., Griesfeller, J., Prospero, J., S. Kinne, S., Bauer, S., Boucher, O., Chin, M., Dentener, F., Diehl, T., Easter, R., Fillmore, D., Ghan, S., Ginoux, P., Grini, A., Horowitz, L., Koch, D., Krol, M., Landing, W., Liu, X., Mahowald, N., Miller, R., J.-Morcrette, J.-J., Myhre, G., Penner, J., Perlwitz, J., Stier, P., Takemura, T., and Zender, C. S.: Global dust model intercomparison in AeroCom phase I, Atmos. Chem. Phys., 11, 7781–7816, https://doi.org/10.5194/acp-11-7781-2011, https://www.atmos-chem-phys.net/11/7781/2011/, 2011.

Jung, E., Albrecht, B., Prospero, J. M., Jonsson, H. H., and Kreidenweis, S. M.: Vertical structure of aerosols, temperature, and moisture associated with an intense African dust event observed over the eastern Caribbean, J. Geophys. Res., 118, 4623–4643, https://doi.org/10.1002/jgrd.50352, 2013.

Kanitz, T., Engelmann, R., Heinold, B., Baars, H., Skupin, A., and Ansmann, A.: Tracking the Saharan Air Layer with shipborne lidar across the tropical Atlantic, Geophys. Res. Lett., 41, 1044–1050, https://doi.org/10.1002/2013GL058780, 2014.

Karyampudi, V. M., Palm, S., Reagen, J., Fang, H., Grant, W., Hoff, R., Moulin, C., Pierce, H., Torres, O., Browell, E., and Melfi, S.: Validation of the Saharan Dust Plume Conceptual Model Using Lidar, Meteosat, and ECMWF Data, Bull. Amer. Meteor. Soc., 80, 1045–1076, https://doi.org/10.1175/1520-0477(1999)080<1045:VOTSDP>2.0.CO;2, 1999.

Kim, D., Chin, M., Yu, H., Diehl, T., Tan, Q., A.Kahn, R., Tsigaridis, K., E.Bauer, S., Takemura, T., Pozzoli, L., Bellouin, N., Schulz, M., Peyridieu, S., Chédin, A., and Koffi, B.: Sources, sinks, and transatlantic transport of North African dust aerosol: A multimodel analysis and comparison with remote sensing data, J. Geophys. Res., 119, 6259–6277, https://doi.org/10.1002/2013JD021099, 2014.

Koffi, B., Schulz, M., Bréon, F.-M., Dentener, F., Steensen, B. M., Griesfeller, J., Winker, D., Balkanski, Y., Bauer, S. E., Bellouin, N., Berntsen, T., Bian, H., Chin, M., Diehl, T., Easter, R., Ghan, S., Hauglustaine, D. A., Iversen, T., Kirkevåg, A., Liu, X., Lohmann, U., Myhre, G., Rasch, P., Ãyvind Seland, Skeie, R. B., Steenrod, S. D., Stier, P., Tackett, J., Takemura, T., Tsigaridis, K., Vuolo, M. R., Yoon, J., and Zhang, K.: Evaluation of the aerosol vertical distribution in global aerosol models through comparison against CALIOP measurements: AeroCom phase II results, J. Geophys. Res., 121, 7254–7283, https://doi.org/10.1002/2015JD024639, https://agupubs.onlinelibrary.wiley.com/doi/abs/10.1002/2015JD024639, 2016.

Kok, J. F.: A scaling theory for the size distribution of emitted dust aerosols suggests climate models underestimate the size of the global dust cycle, Proc. Natl Acad. Sci., 108, 1016–1021, 2011.

Kok, J. F., Mahowald, N. M., Fratini, G., Gillies, J. A., Ishizuka, M., Leys, J. F., Mikami, M., Park, M. S., Park, S. U., Pelt, R. S. V., and Zobeck, T. M.: An improved dust emission model - Part 1: Model description and comparison against measurements, Atmos. Chem. Phys., 14, 13 023–13 041, 2014.

Kok, J. F., Ridley, D. A., Zhou, Q., Miller, R. L., Zhao, C., Heald, C. L., S.Ward, D., Albani, S., and Haustein, K.: Smaller desert dust cooling estimated from analysis of dust size and abundance, Nature Geo., 10, https://doi.org/10.1028/ngeo2912, 2017.

Kramer, S., Kirtman, B., Zuidema, P., and Ngan, F.: Sub Seasonal Variability of Extreme Dust Events over South Florida, J. Geophys. Res., 125, https://doi.org/10.1029/2019JD031874, e2019JD031874, 2020.

Lawson, D. R.: Impaction surface coatings intercomparison and measurements with cascade impactors, Atmos. Environ., 14, 195–199, 1980.

Li-Jones, X. and Prospero, J. M.: Variations in the size distribution of non-sea-salt sulfate aerosol in the marine boundary layer at Barbados: Impact of African dust, J. Geophys. Res., 103, 16 073–16 084, 1998.

Liu, D., Wang, Y., Wang, Z., and Zhou, J.: The three-dimensional structure of transatlantic african dust transport: A new perspective from CALIPSO LIDAR measurements, Adv. Meteor., 2012, https://doi.org/10.1155/2012/8507074, 2012.

Maring, H., Savioe, D. L., Izaguirre, M. A., Custals, L., and Reid, J. S.: Vertical distributions of dust and sea-salt aerosols over Puerto Rico during PRIDE measured from a light aircraft, J. Geophys. Res., 108, 8587–8598, https://doi.org/10.1029/2002JD002544, 2003a.

Maring, H., Savoie, D. L., Izaguirre, M. A., Custals, L., and Reid, J. S.: Mineral dust aerosol size distribution change during atmospheric transport, J. Geophys. Res., 108, 8592–8603, https://doi.org/10.1029/2002JD002536, 2003b.

15 Ott, D. K., Cyrs, W., and Peters, T. M.: Passive measurement of coarse particulate matter PM10-2.5, J. Aer. Sci., 39, 156–167, 2008.

Perry, K. D., Cahill, T. A., Eldred, R. A., Dutcher, D. D., and Gill, T. E.: Long-range transport of North African dust to the eastern United States, J. Geophys. Res., 102, 11,225–11,238, 1997.

Prospero, J. M.: Long-term measurements of the transport of African mineral dust to the eastern United States: Implications for regional air quality, J. Geophys. Res., 104, 15 917–15 927, 1999a.

20 Prospero, J. M.: Assessing the Impact of Advected African Dust on Air Quality and Health in the Eastern United States, Human Ecological Risk Assess.: An Int. J., 5, 471–479, http://dx.doi.org/10.1080/10807039.1999.10518872, 1999b.

Prospero, J. M., Olmez, I., and Ames, M.: Al and Fe in PM 2.5 and PM 10 suspended articles in south-central Florida: The impact of the long range transport of African mineral dust, Water, Air, Soil Pollution, 125, 291–317, 2001.

Randles, C. A., da Silva, A. M., Buchard, V., Colarco, P. R., Darmenov, A., Govindaraju, R., Smirnov, A., Holben, B., Ferrare, R., Hair,
25 J., Shinozuka, Y., and Flynn, C. J.: The MERRA-2 Aerosol Reanalysis, 1980 Onward. Part I: System Description and Data Assimilation Evaluation, J. Climate, 30, 6823–6850, https://doi.org/10.1175/JCLI-D-16-0609.1, https://doi.org/10.1175/JCLI-D-16-0609.1, 2017.

Reid, E. A., Reid, J. S., Meier, M. M., Dunlap, M. R., Cliff, S., and et al., A. B.: Characterization of African dust transported to Puerto Rico by individual particle and size segregated bulk analysis, J. Geophys. Res., 108, https://doi.org/10.1029/2002JD002935, 2003a.

Reid, J. S., Westphal, D. L., Livingston, J. M., Savoie, D. L., Maring, H., Jonsson, H., Eleuterio, D., Kinney, J., and Reid,
30 E.: Dust vertical distribution in the Caribbean during the Puerto Rico Experiment, Geophys. Res. Lett., 29, 1151–1155, https://doi.org/10.1029/2001GL014092, 2002.

Reid, J. S., Jonssonn, H. J., Maring, H. B., Smirnov, A., Savoie, D. L., Cliff, S. S., Reid, E., Livingston, J., Meier, M., Dubovik, O., and Tsay, S.-C.: Comparison of size and morphological measurements of coarse mode dust particles from Africa, J. Geophys. Res., 108, https://doi.org/10.1029/2002JD002485, 2003b.

35 Reid, J. S., Kinney, J., Westphal, D., Holben, B., Welton, E. J., Tsay, S.-C., Eleuterio, D. P., Campbell, J. R., Christopher, S. A., Colarco, P. R., Jonsson, H. H., Livingston, J. M., Maring, H. B., Meier, M. L., Pilewskie, P., Prospero, J. M., Reid, E. A., Remer, L. A., Russell, P. B., Savoie, D. L., Smirnov, A., and Tanre, D.: Analysis of measurements of Saharan dust by airborne and ground-based remote sensing methods during the Puerto Rico Dust Experiment (PRIDE), J. Geophys. Res., 108, 8586–8599, https://doi.org/10.1029/2002JD002493, 2003c.

Ryder, C. L., Highwood, E. J., Lai, T., Sodemann, H., and Marsham, J. H.: Impact of atmospheric transport on the evolution of microphysical and optical properties of Saharan dust, Geophys. Res. Lett., 40, 2433–2438, https://doi.org/10.1002/grl.50482, 2013.

Ryder, C. L., Highwood, E. J., Walser, A., Seibert, P., Philipp, A., and Weinzierl, B.: Coarse and Giant Particles are Ubiquitous in Saharan
5 Dust Export Regions and are Radiatively Significant over the Sahara, Atmos. Chem. Phys. Discuss., https://doi.org/10.5194/acp-2019-421, 2019.

Sauter, K., L'Ecuyer, T., van den Heever, S. C., Twohy, C., Heidinger, A., and Wood, N.: The observed influence of tropical convection on the Saharan dust layer, J. Geophys. Res., 124, 10,896–10,912, https://doi.org/10.1029/2019JD031365, 2019.

Savoie, D. L. and Prospero, J.: Particle size distribution of nitrate and sulfate in the marine atmosphere, Geophys. Res. Letts., 9, 1207–1210,
10 1982.

Savoie, D. L., Prosperoa, J., and Saltzman, E.: Non-sea-salt sulfate and nitrate in tradewind aerosols at Barbados: Evidence for long-range transport, J. Geophys. Res., 94, 5069–5080, 1989.

Shi, H., Xiao, Z., Zhan, X., Ma, H., and Tian, X.: Evaluation of MODIS and two reanalysis aerosol optical depth products over AERONET sites, Atmos. Res., 220, 75–90, 2019.

15 Stein, A. F., Draxler, R., Rolph, G., Stunder, M., Cohen, M., and Ngan, F.: NOAA's HYSPLIT Atmospheric Transport and Dispersion Modeling System, Bull. Am. Meteor. Soc., 96, 2059–2078, https://doi.org/10.1175/BAMS-D-14-00110.1, 2015.

Sugimoto, N. and Lee, C. H.: Characteristics of dust aerosols inferred from lidar depolarization measurements at two wavelengths, Appl. Opt., 45, 7468–7474, 2006.

Tegen, I. and Lacis, A.: Modeling of particle size distribution and its influence on the radiative properties of mineral dust aerosol, J. Geophys.
20 Res., 101, D14, 19 237–19 244, https://doi.org/10.1029/95JD03610, 1996.

v.d. Does, M., Brummer, G.-J., v. Crimpen, F., Korte, L., Mahowald, N., Merkel, U., Prospero, J., Yu, H., Zuidema, P., and Stuut, J.-B.: Tropical rains controlling deposition of Saharan dust across the North Atlantic Ocean, Geophys. Res. Lett., 47, https://doi.org/10.1029/2019GL086867, e2019GL086867, 2020.

Wagner, J. and Leith, D.: Passive aerosol sampler. Part I: Principle of operation, Aerosol Sci. Tech., 34, 186–192, 2001.

25 Wang and John: Comparative bounce properties of particle materials, Aerosol Sci. Technol., 7, 285–299, 1987.

Weinzierl, B., Ansmann, A., Prospero, J., Althausen, D., Benker, N., Chouza, F., Dollner, M., Farrell, D., Fomba, W., Freudenthaler, V.,
580 Gasteiger, J., Groß, S., Haarig, M., Heinold, B., Kandler, K., Kristensen, T., Mayol-Bracero, O., Müller, T., Reitebuch, O., .Sauer, Schäfler, A., Schepanski, K., Spanu, A., Tegen, I., Toledano, C., and Walser, A.: The Saharan Aerosol Long-range Transport and Aerosol-Cloud-Interaction Experiment (SALTRACE) overview and selected highlights, Bull. Amer. Meteor. Soc., https://doi.org/10.1175/BAMS-D-15-00142.1, 2016.

Wilson, R. and Spengler, J.: Particles in Our Air: Concentrations and Health Effects, Harvard University Press, 1996.

585 Yang, W., Marshak, A., Kostinski, A., and Várnai, T.: Shape-induced gravitational sorting of Saharan dust during transatlantic voyage: Evidence from CALIOP lidar depolarization measurements, Geophys. Res. Lett., 40, 3281– 3286, https://doi.org/10.1002/grl.50603., 2013.

Zuidema, P., Alvarez, C., Kramer, S. J., Custals, L., Izaguirre, M., Sealy, P., Prospero, J. M., and Blades, E.: Is summer African dust arriving earlier to Barbados? The updated long-term in-situ dust mass concentration records from Ragged Point, Barbados and Miami, Florida,
590 Bull. Am. Meteor. Soc., https://doi.org/BAMS-D-18-0083.1, 2019.

Table 1. Particle geometric diameter range applied within the GEOS-5 dust size parameterization, corresponding mass extinction efficiencies (MEE) at 550 nm wavelength assuming non-spherical optics (Colarco et al., 2014), and Miami impactor thresholds, in both aerodynamic and geometric diameters (D_a and D_g), where $D_g=0.75D_a$ (Kok et al., 2014).

density kg m^{-3}	GEOS-5 FP μm (D_g)	MEE m^2 g^{-1}	Miami μm (D_a)	Miami μm (D_g)
2500	0.2-2.0	2.02	< 2.1	< 1.575
2650	2.0-3.6	0.64	2.1-4.2	1.575-3.15
2650	3.6-6.0	0.33	4.2-10.2	3.15-7.65
2650	6.0-12.0	0.17	>10.2	> 7.65
2650	12.0-20.0	0.08	NA[1]	NA[1]

[1] not available

Table 2. Measured size of imaged particles in Fig. 10.

particle[1]	longest axis L, μm	longest perpendicular axis; W, μm	aspect ratio L/W	aerodynamic diameter; μm
a1	27.1	12.2	2.2	13.2
a2	17.2	12.4	1.4	10.1
b	36.4	28.8	1.3	20.1
c	27.4	14.1	1.9	13.3
d	21.1	8.1	2.6	10.1

[1] indicated by panel label and image number
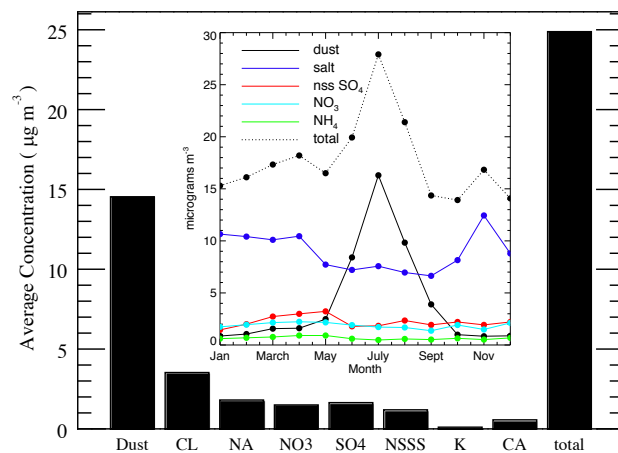
Figure 1. Average aerosol concentrations for July - August 2014 of the soluble ions chlorine (CL), sodium (NA), nitrate (NO3), sulfate (SO4), and non-sea-salt sulfate (NSSS), potassium (K), and calcium (CA). Inset plot is the Miami monthly-mean aerosol concentration by species from 1989 through 1996, replotted from Prospero (1999a).
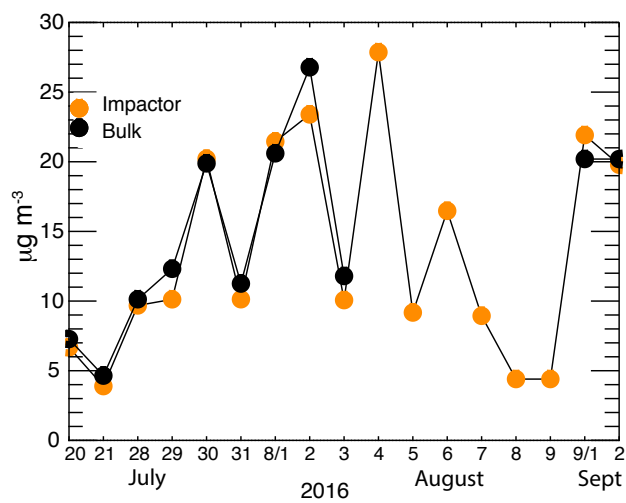
Figure 2. Daily bulk filter dust mass concentrations (black filled circles) and the sum of the impactor dust mass concentrations (orange filled circles) for 20 July - 2 September, 2016 (17 days total). No bulk mass concentration data are available for 4-9 August. Statistically-significant correlation coefficient of 0.98.
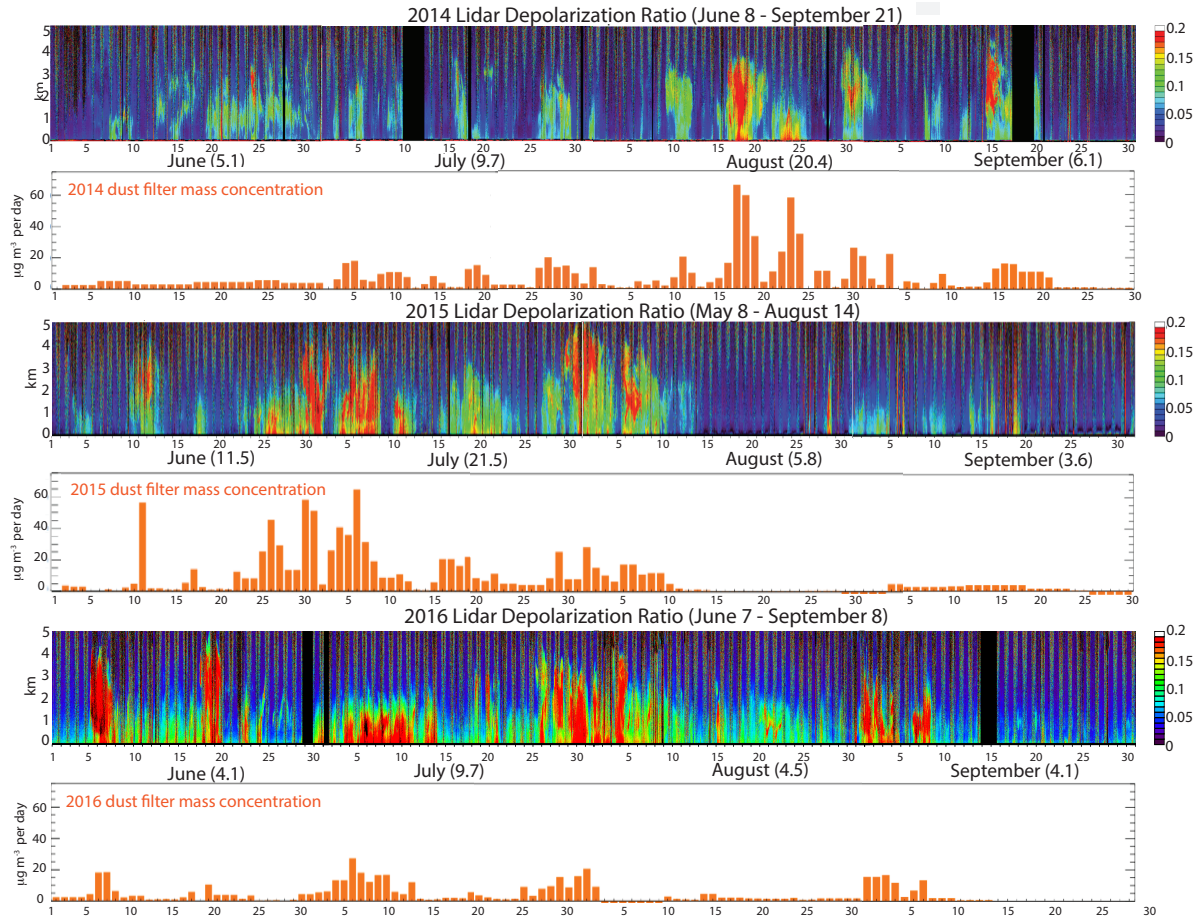
Figure 3. Time series of the MPL volume linear depolarization ratios for June-September, 2014, 2015, 2016, interspersed with the corresponding time series of the daily filter-retrieved bulk dust mass concentrations (units of μg m^{-3} day^{-1}). Subjectively-determined dates of the first and last days with significant dust are indicated within the lidar panel titles. Monthly-mean surface dust mass concentrations (units of μg m^{-3}) are indicated for each month.
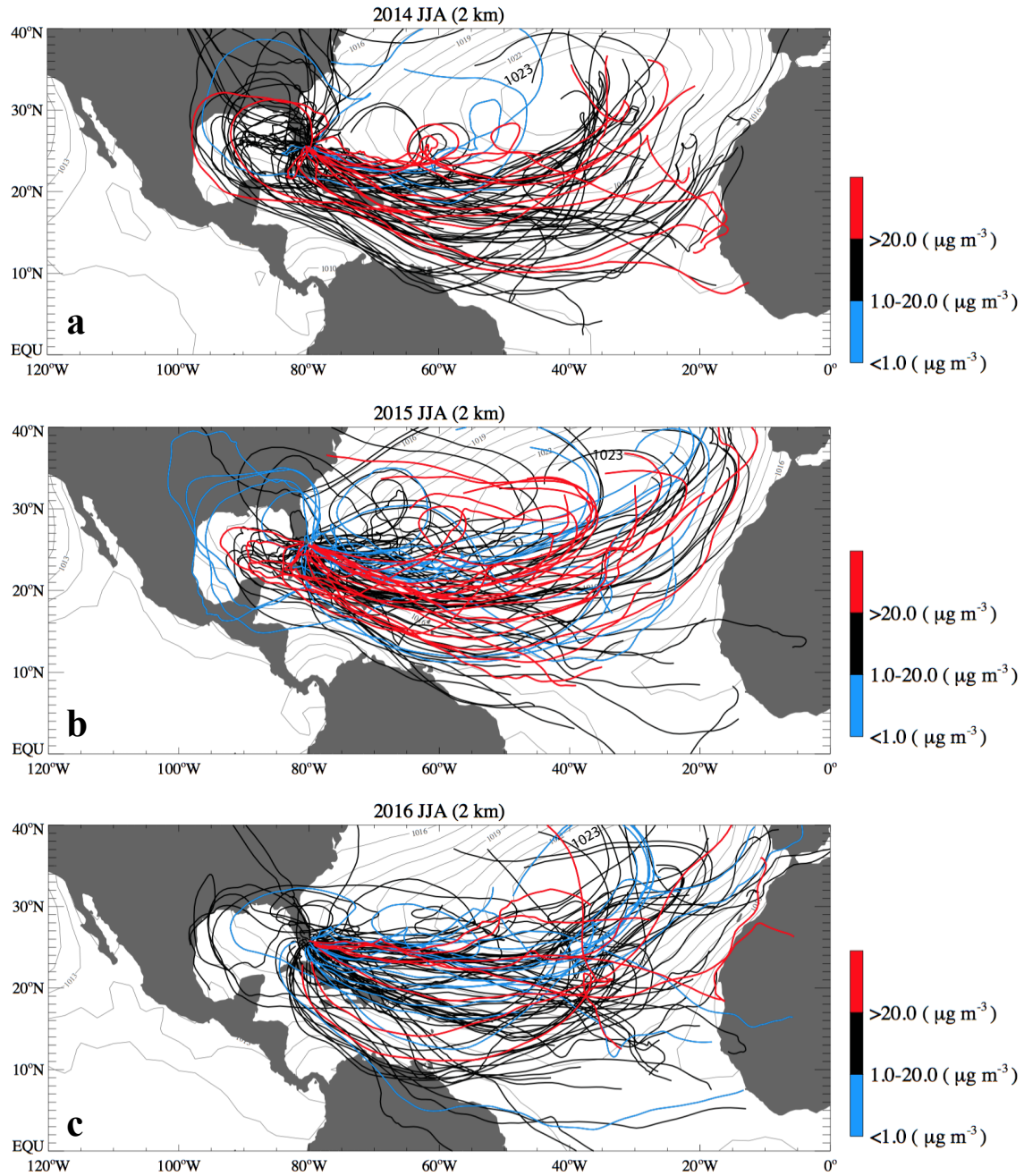
Figure 4. Daily HYSPLIT back trajectories for June-August of a) 2014, b) 2015, and c) 2016, extending for 300 hours and initialized at a height of two km above sea level, with the average seasonal NCEP Reanalysis sea level pressure (grey contours). Back trajectories are color-coded by the dust mass concentrations measured at Miami: initially exceeding> 20 μg m^{-3} (red), 1 - 20 μg m^{-3} (dark blue), and < 1 μg m^{-3} (light blue).
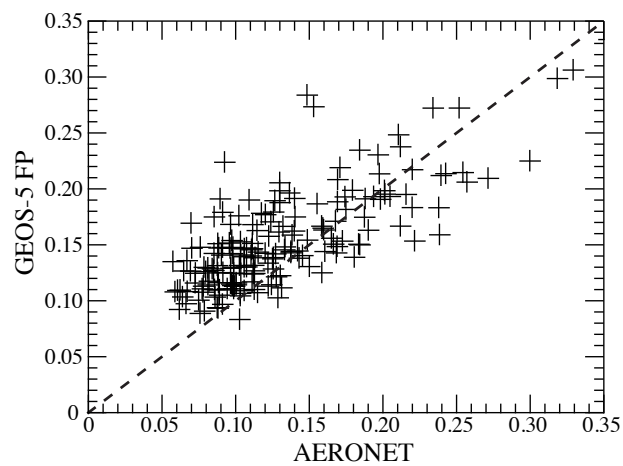
Figure 5. Daily-mean GEOS-5 FP aerosol optical depths τ_{550} versus AERONET-derived values τ_{500} (Level 1.5 version 2) at 500 nm wavelength, for June-September 2015 and 2016. Correlation coefficient of 0.80.
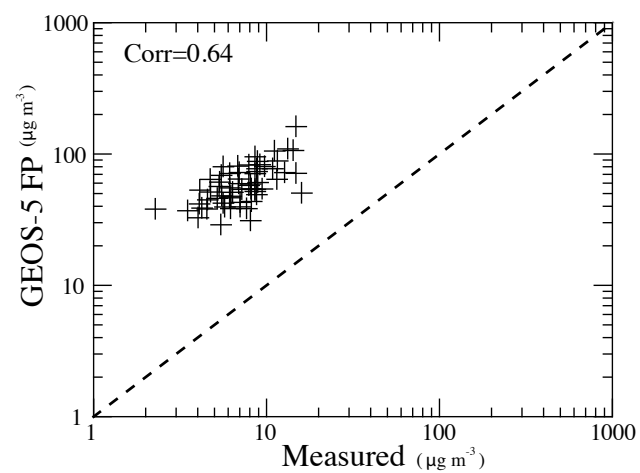
Figure 6. Daily-mean GEOS-5 FP versus measured near-surface salt mass concentrations for July-August, 2014 (32 days). The measured sea salt concentration is computed from the sodium concentration multiplied by 3.256, following Prospero (1999a).
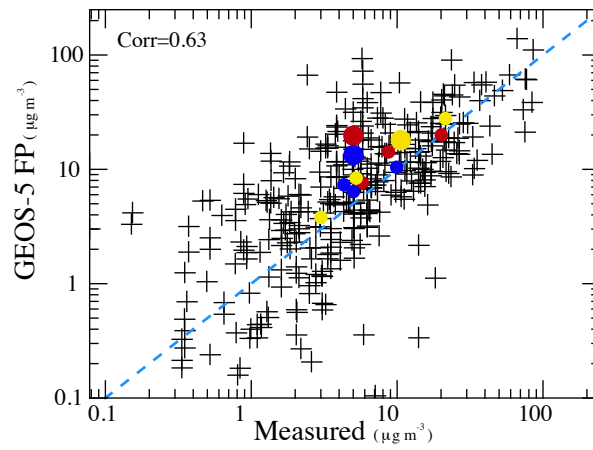
Figure 7. Daily-mean GEOS-5 FP versus measured near-surface dust mass concentrations for June-September from 2014-2016 (366 days), with monthly-mean values superimposed for 2014 (dark red), 2015 (dark yellow) and 2016 (blue); a larger filled circle highlights June. y=x line indicated. Correlation (in logarithmic space) of 0.63.
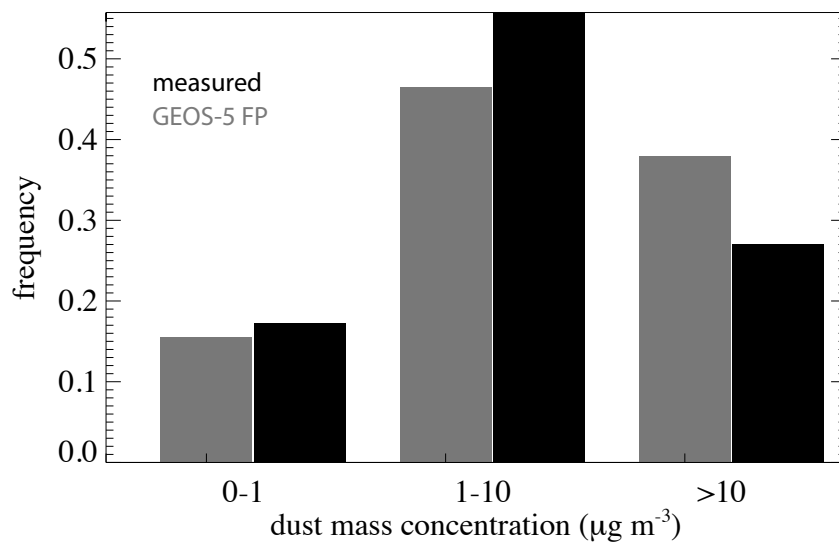
Figure 8. Frequency of days with measured (black) and model (grey) daily-mean dust mass concentrations in three diameter bins, based on 366 days from June-September, 2014-2016.
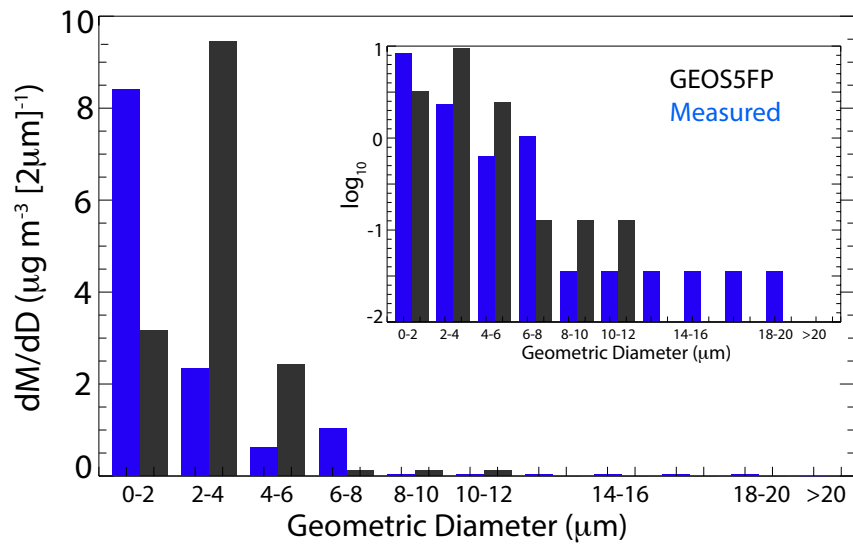
Figure 9. 17-day-average dust mass concentration per (two μm)$^{-1}$ geometric diameter bin from measurements (blue) and GEOS-5 FP (black).
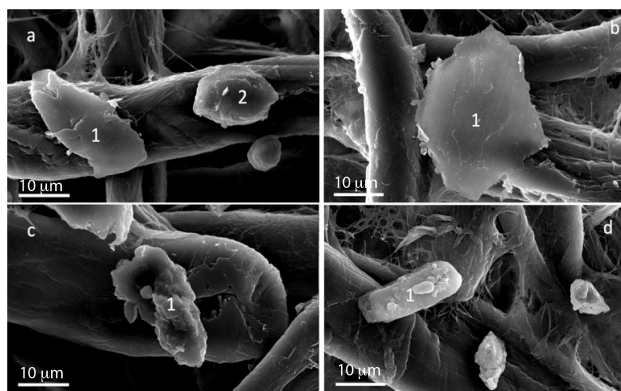
Figure 10. Scanning electron microscopy images of filter samples from a) and b) August 1, 2016, and c) and d) August 2, 2016. Individual particle dimensions are shown in Table 2. The cellulose filter fibers used for collection are visible in the background behind each particle.
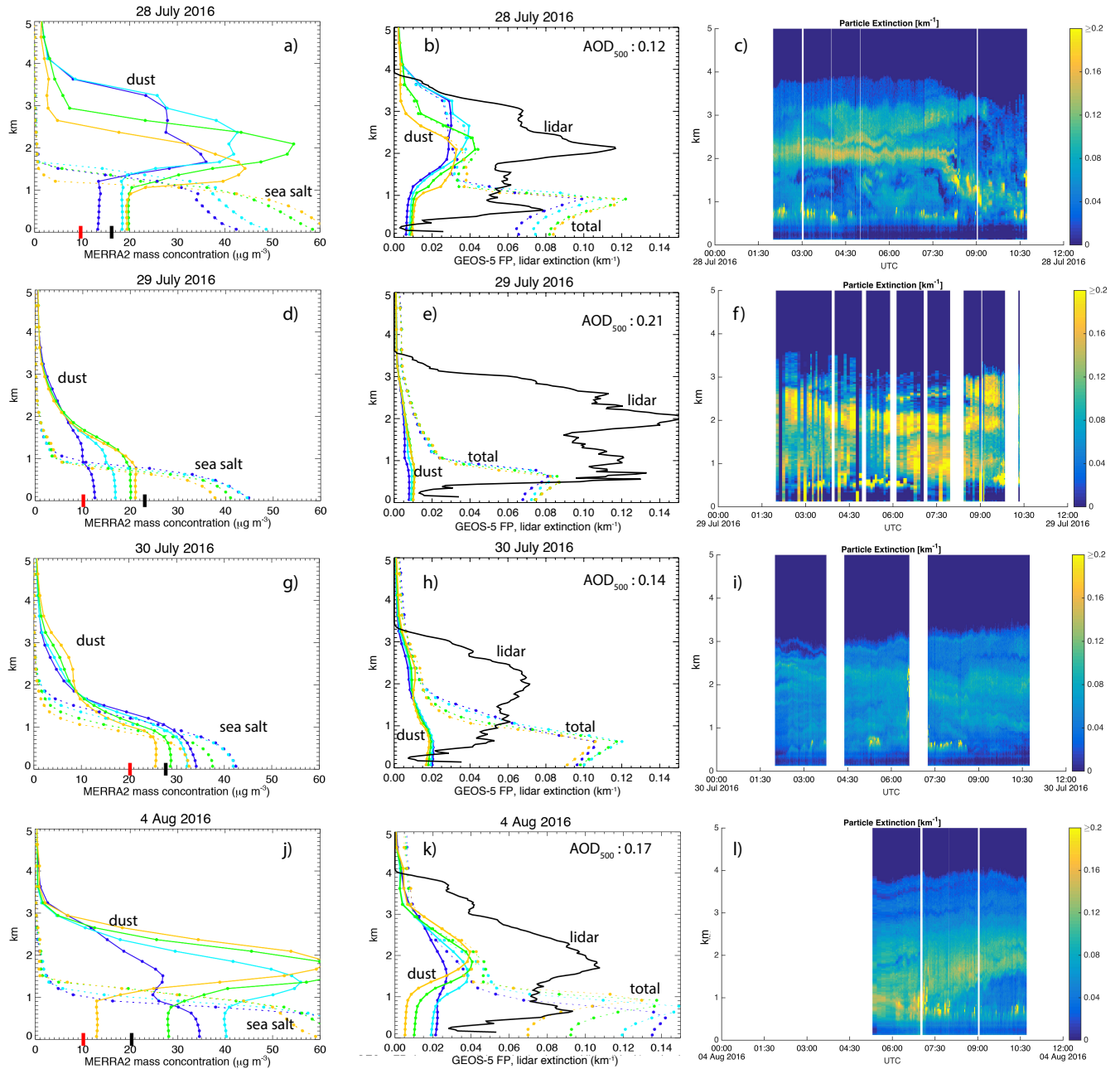
Figure 11. a) MERRA-2 dust (solid) and sea salt (dashed) mass concentrations for 28 July 2016 3-12 UTC (dark blue, light blue, green and yellow lines indicate 3, 6, 9, and 12 UTC respectively), with surface model (black) and impactor (red) total dust mass concentrations included as thick vertical lines. b) GEOS-5 FP dust (solid) and total (dashed) volume extinction coefficients for 28 July 2016 3-12 UTC (same labeling scheme as in a)) and the lidar-derived volume extinction coefficient profile averaged over cloud-free portions (determined visually from camera imagery) of 28 July 2-11 UTC (black). The average 11-13 UTC AERONET-derived aerosol optical depth at 500 nm is indicated. c) 28 July 2011 UTC lidar-derived volume extinction coefficient time series. d)-f) same as a)-c) but for 29 July 2016. g)-i) same as a)-c) but for 30 July 2016. j)-l) same as a)-c) but for 5 August 2016. 3-12 UTC corresponds to 19-7 local time.
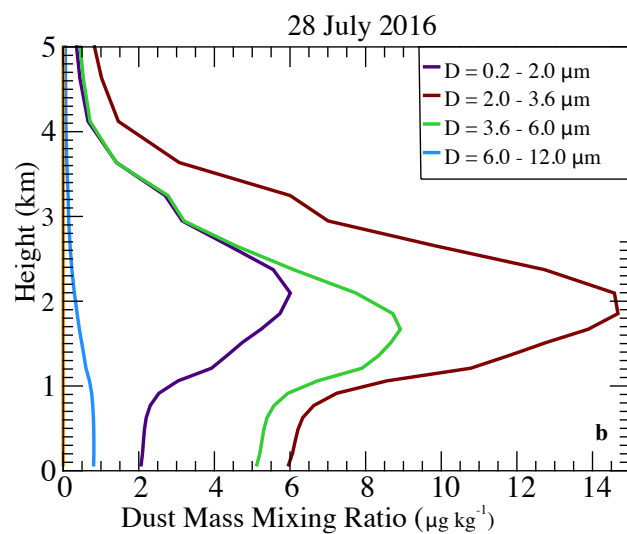
Figure 12. Size-resolved GEOS-5 FP dust mass mixing ratio vertical profiles for 28 July, 2016.